Accurate Loop Gain Model of Ripple-Based Constant on-time Controlled Buck Converters

Danzhu Lu, *Senior Member, IEEE*, Xiaoyang Zeng, *Senior Member, IEEE*, and Zhiliang Hong, *Senior Member, IEEE*

***Abstract*—Ripple based constant on-time (RBCOT) control has been widely used in dc–dc buck converters over past years. However, there has been no accurate loop gain model to link the property of RBCOT controlled buck converter to existing knowledge about basic feedback control principles like crossover frequency (Fc) and phase margin so far. The previously reported stability criterion for the output capacitor's equivalent series-resistor, i.e., Ton/(2C), is insufficient to avoid subharmonic oscillations over all duty cycle values. This article presents a new accurate loop gain model for the RBCOT control. Without simplification, the proposed model can accurately predict the system response even beyond the switching frequency. The proposed modeling approach has been extended to two types of external ramp compensation schemes (for solving the subharmonic oscillation issue) and optimum ranges of ramp compensation amplitudes have been derived accordingly. The modeling results are verified by the SIMPLIS simulations and experimental results.**

***Index Terms*—Constant on-time control, design guideline modeling, external ramp compensation, ripple-based control modeling.**

I. Introduction

RIPPLE-BASED constant on-time (RBCOT) control scheme has been widely applied in point-of load buck converters and voltage regulator modules due to the increasing demands for fast transient response and simple compensation [1], [2], [3], [4], [5], [6], [7], [8], which are critical for processors and computer system applications. As shown in Fig. 1(a), an integral cell composed by an error amplifier (EA) and a compensation capacitor (Cc) is added in V^2 RBCOT control to introduce an outer integral loop and then eliminate the dc error caused by output ripple [2]. However, the RBCOT control using equivalent series-resistor (ESR) ripple as the pulsewidth modulation (PWM) ramp may suffer from the subharmonic oscillation instability when ceramic capacitors with small ESR is employed.

External ramp compensation has been preferred to alleviate the subharmonic oscillation and guarantee the system stability even with small ESR ripple. As shown in Fig. 1(b) and (c), major ramp compensation methods can be divided into two categories: Fixed slope ramp compensation [1], [2] and inductor current (IL) related ramp compensation [3], [4], [5], [6], [7]. For fixed slope ramp compensation methods, external fixed slope ramp Sr is added to V_c and compared with the output voltage to trigger the PWM signal. Since the slope is fixed, no inductor current sensing is required. However, for large duty cycle applications, the fixed slope ramp compensation cannot achieve proper damping for the control loop, which may lead to instability and poor transient performance [9]. To solve this problem, the IL related ramp compensation Sr can be added to the output ripple and their sum is compared with V_c to trigger the PWM signal. If the dc value of IL is included in $V_{\rm ramp}$, the dc value of V_c need to be changed

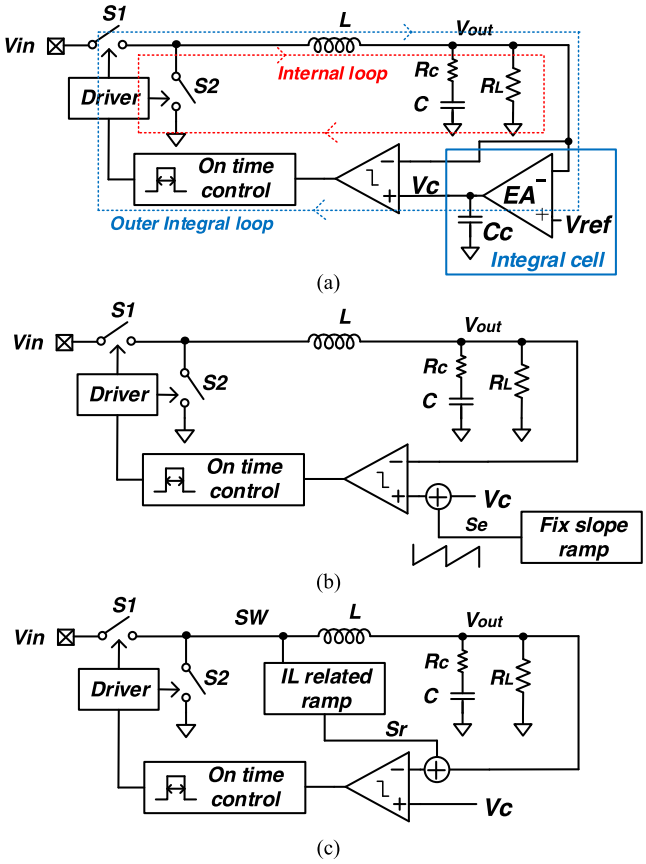

Fig. 1. Architecture of the RBCOT control with (a) V^2 control, (b) fixed slope ramp, and (c) IL related ramp.

Manuscript received 19 September 2022; revised 23 January 2023; accepted 3 March 2023. Date of publication 10 March 2023; date of current version 20 April 2023. Recommended for publication by Associate Editor M. Rodríguez. *(Corresponding author: Zhiliang Hong.)*

The authors are with the State Key Laboratory of Integrated Chips and Systems, School of Microelectronics, Fudan University, Shanghai 201203, China (e-mail: lvdanzhu@fudan.edu.cn; xyzeng@fudan.edu.cn; zlhong@fudan.edu.cn).

Color versions of one or more figures in this article are available at https://doi.org/10.1109/TPEL.2023.3254906.

Digital Object Identifier 10.1109/TPEL.2023.3254906

during load transition, which will result in an undesirable output voltage droop. Therefore, it is preferred to use only the ac portion of the IL ripple for compensation. The output capacitor current ripple is a kind of the ac IL ramp, but the impedance of the current sensing network must be proportional to the impedance of output capacitor to achieve proper compensation [3], [4], [5]. The ac IL ramp compensation could also be generated by adding a RC filter to the SW node [6], [7].

The small signal modeling of V^2 controlled buck converter is not straight forward due to the complexity of the nonlinear PWM modulator. Since the output switching-frequency ripple voltage is directly involved in the duty-cycle modulation of RBCOT control, the traditional continuous-time (CT) small-signal average model [10] which neglects the effects of output ripple becomes less effective here. To overcome the limitation of the average-time model, other modeling methods like sample-date modeling [11], [12], [13], [14], Krylov–Bogoliubov–Mitropolsky (KBM) method [15], and discrete-time (DT) modeling [16], [17], [18], [19], [20] were proposed one after another. In the early days, the ripple-based control was considered as a simplified implementation of current mode control saving a discrete current sensing resistor. Therefore, the sampled-data modeling techniques [11], [12], [13] were employed to derive the stability criterion. However, it has been proved that the sample and hold concept is not applicable to variable frequency modulations [21], and thus the analysis results were not satisfactory. Although all the side-band components of the feedback signal are included in the sampled-data modeling [14], the final stability criterion is the same as that in [13] and no design guideline can be provided with a certain stability margin. The KBM ripple estimation technique [15] has been utilized to predict the influence of the capacitor voltage ripple and the effect of the external ramp in constant frequency V^2 control, but the tedious algebraic calculations is a challenge to the engineers trying to extend it to variable frequency controls. DT models based on Jacobian matrix analysis [16], [17], [18], Bifurcation analysis [17], [18], [19], and Floquet theory [20] were applied to RBCOT buck converters with ESR ramp or IL related ramp compensation to derive the accurate stability boundary and complex dynamical behaviors. However, most DT analyses provide very little physical insight since they are based on numerical analysis and no symbolic expression can be extracted. Moreover, an absolute instability boundary does not fully characterize the frequency domain behavior of a ripple-based controlled converter, such as phase margin (PM) and crossover frequency (Fc) of the loop gain. Therefore, a design-oriented model in the conventional frequency domain is highly desired for engineers to design the RBCOT controlled converters and compare them with converters employing other control schemes, such as the current mode or the voltage mode controls.

Describing function (DF) method based on time-domain waveform is one successful CT model for small-signal analysis. It provides a good model for nonlinear current-mode modulator in constant on-time current mode (COTCM) control [22], [23] and an accurate transfer function from the control signal to the output voltage is obtained. However, when applying the DF method to the V^2 control, only the transfer function from the control signal (Vc) to the output voltage (Vout) was obtained in previous works [2], [24], [25], which is difficultly verified because the point of measurement is usually not physically accessible due to integrated circuit implementation of the control circuits [26]. Moreover, the control to the output transfer function could not provide sufficient physical insights since all building blocks including power stage and the PWM comparator are lumped together. Therefore, previous DF analyses fail to relate the properties of V^2 control to the loop gain, which is defined as the product of the small-signal gains in the forward and feedback paths of the feedback loop. The properties of loop gain like Fc and PM have been widely used in voltage mode [10] and current mode [27] controlled buck convertors to predict their stability and their behavior of load/line transient response. However, no analytical expressions are available for Fc and PM in RBCOT controlled buck converter so far.

Furthermore, in previous reported simplified control to output transfer function as shown below [24]

$$\frac{v_{\text{out}}(s)}{v_c(s)} = \frac{(1+sR_CC)}{\left(1+\frac{s}{Q_1\omega_1}+\frac{s^2}{\omega_1^2}\right)\left(1+\frac{s}{Q_3\omega_2}+\frac{s^2}{\omega_2^2}\right)} = \frac{T(s)}{1+T(s)} \tag{1}$$

where $T(s)$ is the loop gain of the control loop. The dc gain of (1) is equal to one, which indicates the dc value of the loop gain is infinite even ESR is very large, which is not reasonable because the output accuracy is poor for such case.

Some design-oriented models [28], [29], [30] have also been proposed, which apply familiar loop gain concepts for the V^2 inner voltage loop by separating the ESR ripple and the output capacitor voltage ripple. The ESR ripple was treated as IL sensing, and then the previous small signal analysis results for the COTCM [31] control can be applied to the V^2 control with lots of simplification. However, the switching ripple of the output capacitor could not be ignored since it will also affect the PWM comparator, in the same way as the ESR ripple, especially near the critical stable point when the output capacitor ripple and ESR ripple have similar amplitudes. Fig. 2 compares the loop gain of the ESR ripple and the IL sensing. They are different even with the same Rc. Therefore, the modeling concept based on the separation of the two kinds of ripples is not practical.

Another questionable assumption of the previous V^2 control modeling efforts with DF method is that the effects of different types of external ramp compensation schemes are treated in the same way. Thus, the stability criteria for the external ramps are assumed to be equivalent as the ESR ramp [24], [25]. However, the loop gain properties of the ESR ripple, the fixed slope ramp compensation and the IL ac ramp compensation with an SW filter are totally different as shown in Fig. 3. It can be seen that both the Fc and PM are different though the PWM ramp slope are the same. Moreover, in the previous small-signal model for the V^2 control the effect of outer integral loop was not discussed in detail. Although the integral cell is included in the small-signal model in [26], no design-oriented analysis is applied to the integral cell.

In the context of RBCOT control modeling, the primary objectives of this article are the following.

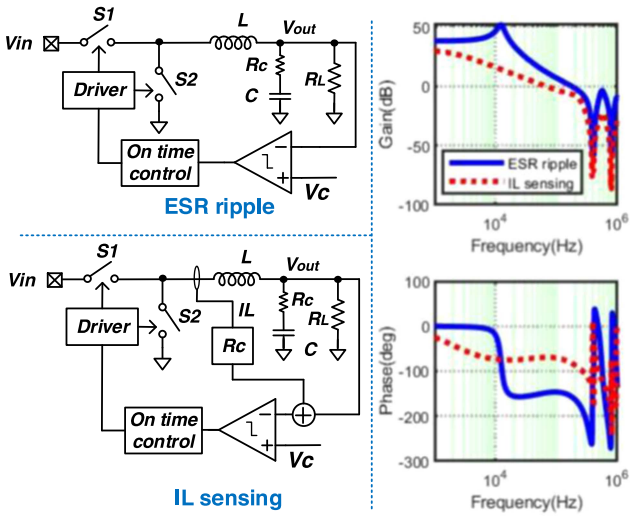

Fig. 2. Comparison of loop gain for the ESR ripple and the IL sensing ($V_{\rm in}$ = 12 V, $V_{\rm out}$ = 5 V, fs = 400 kHz, C = 250 μF, L = 660 nH, and Rc = 10 mΩ).

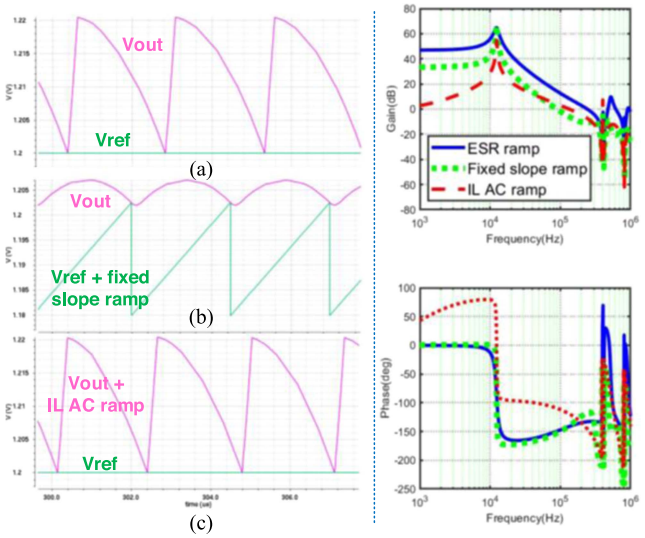

Fig. 3. Loop gain SIMPLIS simulation results for (a) ESR ripple (b) fixed slope ramp (c) IL ac ramp with SW filter ($V_{\rm in}$ = 12 V, $V_{\rm out}$ = 1.2 V, fs = 400 kHz, C = 250 μF, L = 660 nH, and effective ESR = 5 mΩ).

1) To derive a design-oriented loop gain model, which is accurate even beyond the switching frequency, for the RBCOT control.
2) To predict the transient response for RBCOT control according to the Fc and PM in loop gain model.
3) To apply a design-oriented analysis for an integral cell based on the loop gain model including an outer integral loop.
4) To extend the loop gain model to the RBCOT controlled converters with the fixed slope ramp compensation and the IL AC ramp compensation.
5) To derive the design guidelines for the external ramp compensation amplitude.

The remaining of this article is organized as follows: In Section II, the RBCOT control with the ESR ripple will be used as an example to illustrate the modeling process. The relationship between stability and the ESR will be revealed in the proposed model. Then, Section III describes the influence of the outer integral loop to the proposed loop gain model. In Section IV, the extensions of this model to the fixed slope ramp compensation and the IL ac ramp compensation are presented. Simulations and experiments are used to verify the proposed model in Section V. Finally, a brief conclusion is given in Section VI.

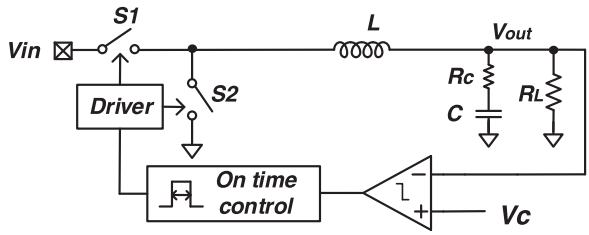

Fig. 4. Buck converter for exemplifying the model.

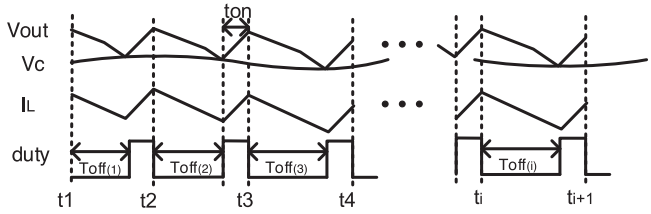

Fig. 5. Waveforms with the V_c perturbation.

II. Proposed Loop Gain Model for RBCOT Control

As shown in Fig. 4, the RBCOT controlled buck converter composed of the switches, the inductor, the output capacitor, the comparator, and the on-time generator is used to exemplify the proposed modeling approach. The integrator represented by EA and Cc in Fig. 1(a) will be neglected firstly in this section. The assumptions of DF method [24] are listed as following to simplify the calculation: the magnitude of the inductor current slopes during the on- and off-periods stay constant separately; the magnitude of the perturbation signal is very small; and the perturbation frequency *fm* and the switching frequency *fs* are commensurable, which means that $N \times fs = M \times fm$, where N and M are both positive integers.

First, the perturbation $r_0 + \hat{r}\sin(\omega_m t - \theta)$ is added to the output of the EA V_c, where $\hat{r}$ is the amplitude of the perturbation. Based on the duty cycle and the output voltage waveforms shown in Fig. 5, it is found that

$$\begin{aligned}\Delta V_{\text{total\_output\_ripple}} &= \Delta V_{\text{ESR\_ripple}} + \Delta V_{\text{Capacitor\_ripple}} \\ &= \left(\Delta I_L - \Delta I_{\text{load}}\right) R_c + \Delta V_{\text{Capacitor\_ripple}} \\ &= \left(s_n T_{\text{on}} - s_f T_{\text{off}(i)}\right) \\ &\quad - \frac{v_c\left(t_i + T_{\text{off}(i)}\right) - v_c\left(t_{i-1} + T_{\text{off}(i-1)}\right)}{R_L} R_c \\ &\quad + \frac{\int_{t_{i-1}+T_{\text{off}(i-1)}}^{t_i+T_{\text{off}(i)}} \left(i_L(t) - \frac{v_o(t)}{R_L}\right) dt}{C_o} \\ &= v_c\left(t_i + T_{\text{off}(i)}\right) - v_c\left(t_{i-1} + T_{\text{off}(i-1)}\right).\end{aligned} \tag{2}$$

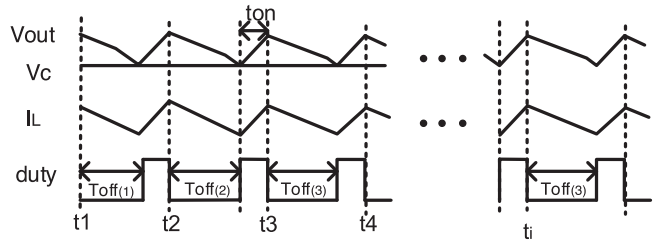

Fig. 6. Waveforms with the V_{out} perturbation.

where $T_{\text{off}(i)}$ is the ith cycle OFF-time, $S_n = R_c \times (V_{\text{in}}\text{-}V_{\text{out}})/L$, $S_f = Rc \times V_{\text{out}}/L$, $i_L(t)$ is the inductor current, and $V_o(t)$ is the output voltage.

Since the V_{out} perturbation is neglected here, $V_o(t) = V_{\text{out}}$ where V_{out} is the steady-state value of the output voltage. Assuming that $T_{\text{off}(i)} = T_{\text{off}} + \Delta T_{\text{off}(i)}$, where T_{off} is the steady-state OFF-time and $\Delta T_{\text{off}(i)}$ is the ith cycle off-time perturbation, then based on (2), the steady-state relationship between Vout and IL can be

$$\begin{aligned} & s_f \Delta T_{\text{off}(i)} \left(1 + \frac{T_{\text{off}}}{2R_cC_o}\right) - s_f \Delta T_{\text{off}(i-1)} \left(1 + \frac{T_{\text{off}} - 2T_{sw}}{2R_cC_o}\right) \\ & = \left(1 + \frac{R_c}{R_L}\right) \left(v_c\left(t_{i-1} + T_{\text{off}(i-1)}\right) - v_c\left(t_i + T_{\text{off}(i)}\right)\right. \\ & \quad \left. - \left(v_c\left(t_{i-2} + T_{\text{off}(i-2)}\right) - v_c\left(t_{i-1} + T_{\text{off}(i-1)}\right)\right)\right) \end{aligned} \tag{3}$$

where T_{sw} is the steady-state switching period which could be expressed as $T_{\text{on}} + T_{\text{off}}$. Based on (3) and the results in [24], the Fourier coefficient of the duty cycle $c_{m(d)}$ at the perturbation frequency f_m can be expressed by

$$c_{m(d)} = \frac{\hat{r}e^{-j\theta}}{2j} \frac{f_s\left(1 - e^{-j\omega_m T_{\text{on}}}\right)\left(1 - e^{-j\omega_m T_{sw}}\right)\left(1 + \frac{R_c}{R_L}\right)}{s_f\left(\left(1 + \frac{T_{\text{off}}}{2R_cC_o}\right) - e^{-j\omega_m T_{sw}}\left(1 + \frac{T_{\text{off}} - 2T_{sw}}{2R_cC_o}\right)\right)}. \tag{4}$$

The Fourier coefficient at the perturbation frequency f_m for $V_c(t)$ is $\hat{r}e^{-j\theta}/2j$; therefore, the transfer function from the control signal to the duty cycle can be calculated as

$$\begin{aligned} F_{dx}(s) &= \frac{d(s)}{v_c(s)} = \frac{c_{m(d)}}{c_{m(vc)}} \\ &= \frac{f_s}{s_f} \frac{\left(1 - e^{-sT_{\text{on}}}\right)\left(1 - e^{-sT_{sw}}\right)\left(1 + \frac{R_c}{R_L}\right)}{\frac{T_{sw}}{R_cC_o} + \left(1 + \frac{T_{\text{off}} - 2T_{sw}}{2R_cC_o}\right)\left(1 - e^{-sT_{sw}}\right)}. \end{aligned} \tag{5}$$

Second, the perturbation $r_0 + \hat{r}\sin(\omega_m t - \theta)$ is added to the output voltage $V_o(t)$ and the V_c perturbation is neglected. Based on the duty cycle and the output voltage waveforms in Fig. 6, it is found that

$$s_n T_{\text{on}} - s_f T_{\text{off}(i)} + \frac{\int_{t_{i-1}+T_{\text{off}(i-1)}}^{t_i+T_{\text{off}(i)}} \left(i_L(t) - \frac{v_o(t)}{R_L}\right) dt}{C_o} = 0. \tag{6}$$

Based on (6) and the steady-state relationship between V_{out} and IL, one can get (7), shown at the bottom of the next page.

A similar Fourier analysis is performed on duty cycle again and the DF from the output voltage to $d(s)$ can be calculated as

$$\begin{aligned} F_{odx}(s) &= \frac{d(s)}{vo(s)} \\ &= \frac{f_s}{s_f} \frac{\left(1 - e^{-sT_{on}}\right)\left(1 - e^{-sT_{sw}}\right)\left[\frac{1}{s^2LC_o} + \frac{\left(\frac{R_c}{L} + \frac{1}{R_LC_o}\right)}{s}\right]}{\frac{T_{sw}}{R_cC_o} + \left(1 + \frac{T_{off} - 2T_{sw}}{2R_cC_o}\right)\left(1 - e^{-sT_{sw}}\right)}. \end{aligned} \tag{8}$$

From (5) and (8), it is clear that the transfer functions from the two inputs of PWM modulator (V_c and V_o) to duty cycle $d(s)$ are different. Therefore, the $F_{\text{odx}}(s)$ can be separated to two parts: one part is the same as $F_{dx}(s)$ which is related to the PWM modulator, the other part $F_{ox}(s)$ including the output ripple directly influencing d(s) according to the control scheme. Therefore, $F_{ox}(s)$ can be expressed as

$$F_{ox}(s) = -F_{odx}(s) - F_{dx}(s). \tag{9}$$

Based on above assumptions, the small signal model for the V^2 RBCOT controlled buck converter can be shown as Fig. 7. Different from previous DF models [26], one additional internal transfer function $F_{ox}(s)$ exists from $\underline{V}_{\text{out}}(s)$ to duty cycle $d(s)$.

$F_p(s)$ is transfer function of the power stage from the duty cycle to V_{out}. It could be expressed as

$$F_p(s) = V_{\text{in}} \frac{1 + sR_cC_o}{1 + s\left(R_cC_o + \frac{L}{R_L}\right) + s^2LC\left(1 + \frac{R_c}{R_L}\right)}. \tag{10}$$

Then, the loop gain of the model from the broken point in Fig. 7 is

$$F_{\text{loop}}(s) = \frac{F_{dx}(s) \times F_p(s)}{1 + F_{ox}(s) \times F_p(s)} \tag{11}$$

where $F_{ox}(s) = -F_{odx}(s) - F_{dx}(s)$. The exponential term e^{-sTsw} can be simplified using the Padé approximation [32] which is valid up to fs/2

$$e^{-sT_{sw}} = 1 - \frac{sT_{sw}}{1 + \frac{sT_{sw}}{2} + \frac{T_{sw}^2}{\pi^2}}.$$

Then, $F_{\text{loop}}(s)$ can be simplified as

$$F_{\text{loop}}(s) = \frac{A_0\left(1 + \frac{s}{\omega_z}\right)}{\left(1 + \frac{s}{Q_2\omega_{p2}} + \frac{s^2}{\omega_{p2}^2}\right)\left(1 + \frac{s}{Q_1\omega_{p1}} + \frac{s^2}{\omega_{p1}^2}\right)} \tag{12}$$

where

$$A_0 = LC_o\left(1 + \frac{R_c}{R_L}\right) / \left[\left(\frac{T_{sw}}{\pi}\right)^2 + \left(\frac{T_{on}}{\pi}\right)^2 + \frac{T_{on}}{2}\left(R_cC_o - \frac{T_{on}}{2}\right)\right]$$

$$\omega_z = 1/R_cC_o$$

$$\omega_{p1} = 1/\sqrt{LC_o\left(1 + R_c/R_L\right)}$$

$$Q_{p1} = 1/\omega_{p1}/\left(C_oR_c + L/R_L\right)$$

$$\omega_{p2} = \pi\sqrt{1 + \pi^2\left(R_cC_o/2/T_{\text{on}} - 1/4\right) + \left(T_{sw}/T_{\text{on}}\right)^2}/T_{sw}$$

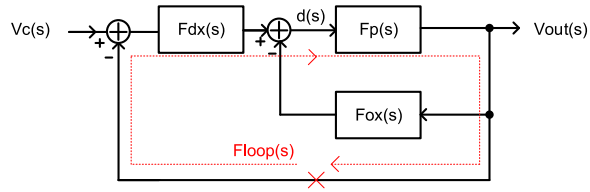

Fig. 7. Small signal model for RBCOT buck converter.

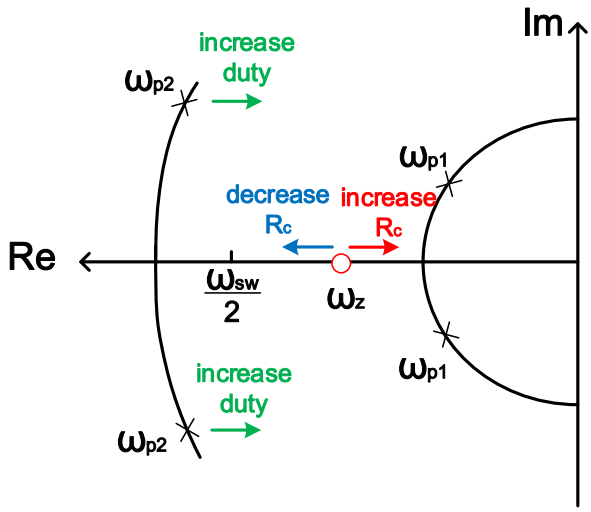

Fig. 8. Root locus diagram of the loop gain.

$Q_{p2} = \sqrt{1+\pi^2(R_cC_o/2/T_{\text{on}} - 1/4) + (T_{sw}/T_{\text{on}})^2}$ /π/ $(R_cC_o/T_{sw} - T_{\text{on}}/2/T_{sw} + T_{sw}/2/T_{\text{on}})$.

The zero ω_z and the double pole ω_{p1} are generated from the power stage. ω_{p2} is related to the duty cycle D which could be expressed as $D = T_{\text{on}}/T_{\text{sw}} = V_{\text{out}}/V_{\text{in}}$. When duty cycle is relatively small, which means V_{out} is much lower than V_{in}, ω_{p2} is higher than switching frequency and its influence on the stability is ignorable. As shown in Fig. 8, a small Rc will push ω_z to high frequency and make the system unstable, while a too large Rc will increase the PM, but introduce large output ripple. Therefore, an optimum Rc exists for the system. Assuming that around the optimum Rc, ω_z does not influence the Fc significantly, the Fc and the PM of $F_{\text{loop}}(s)$ can be simplified as

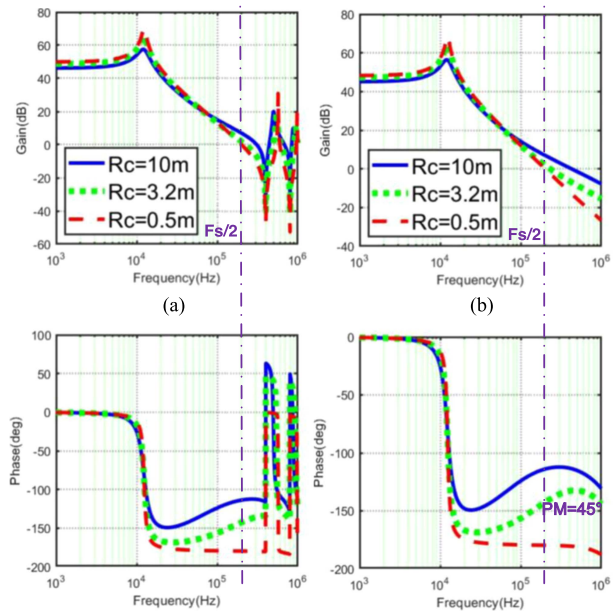

Fig. 9. Loop gain for different ESR ($V_{\text{in}} = 12$ V, $V_{\text{out}} = 1.2$ V, fs = 400 kHz, C = 250 μF, $L = 660$ nH). (a) Without approximants. (b) With approximants.

$$\omega_c = 2\pi F_c \approx \sqrt{A_0}\,\omega_{p1} = \frac{1}{\sqrt{\left(\frac{T_{sw}}{\pi}\right)^2 + \left(\frac{T_{\text{on}}}{\pi}\right)^2 + \frac{T_{\text{on}}}{2}\left(R_cC_o - \frac{T_{\text{on}}}{2}\right)}} \tag{13}$$

$$PM \approx \arctan\left(\omega_c/\omega_z\right) \tag{14}$$

where ω_c is the angular frequency of Fc. Assuming that PM $>$ 45° is needed for stable operation, if the duty cycle is less than 20%, the optimum Rc could be obtained as $R_c = \frac{T_{sw}}{\pi C_o}$ according to (14). ω_z is equal to ω_c for this optimum R_c, which meets the above assumptions. If the duty cycle is larger than 50%, ω_{p2} will close to ω_c so a larger Rc is required to guarantee enough PM. The optimum Rc is then around $\frac{4T_{sw}}{C_o}$.

The bode diagrams of proposed loop gain model with different Rc are shown in Fig. 9. We can find that the Padé Approximants can guarantee the modeling accuracy up to half of the switching

$$\begin{aligned}
&s_f\Delta T_{\text{off}(i)}\left(1+\frac{T_{\text{off}}}{2R_cC_o}\right) - s_f\Delta T_{\text{off}(i-1)}\left(1+\frac{T_{\text{off}}-2T_{sw}}{2R_cC_o}\right)\\
&= \frac{\left(\frac{R_c}{L}+\frac{1}{R_LC_o}\right)}{\omega_m}\left(\hat{v}_o\left(t_i+T_{\text{off}(i)}+\frac{\pi}{2\omega_m}\right) - \hat{v}_o\left(t_{i-1}+T_{\text{off}(i-1)}+\frac{\pi}{2\omega_m}\right)\right.\\
&\left. - \left(\hat{v}_o\left(t_{i-1}+T_{\text{off}(i-1)}+\frac{\pi}{2\omega_m}\right) - \hat{v}_o\left(t_{i-2}+T_{\text{off}(i-2)}+\frac{\pi}{2\omega_m}\right)\right)\right)\\
&+ \frac{\left(\hat{v}_o\left(t_i+T_{\text{off}(i)}\right)-\hat{v}_o\left(t_{i-1}+T_{\text{off}(i-1)}\right)\right)-\left(\hat{v}_o\left(t_{i-1}+T_{\text{off}(i-1)}\right)-\hat{v}_o\left(t_{i-2}+T_{\text{off}(i-2)}\right)\right)}{\omega_m^2 LC_o}.
\end{aligned} \tag{7}$$

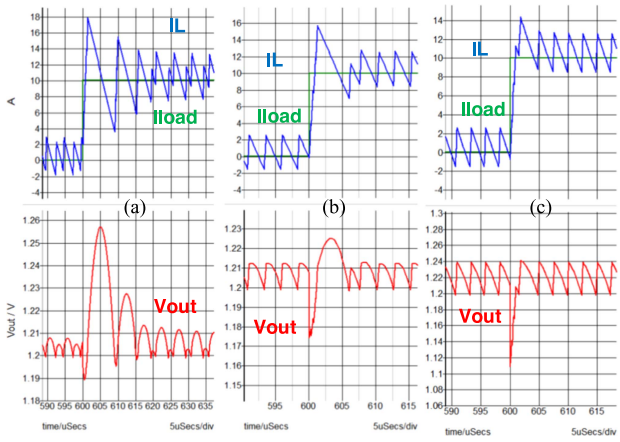

Fig. 10. Load transition for different ESR ($V_{\rm in}$ = 12 V, $V_{\rm out}$ = 1.2 V, fs = 400 kHz, C = 250 μF, L = 660 nH). (a) Rc = 1 mΩ. (b) Rc = 3.2 m Ω. (c) Rc = 10 mΩ.

frequency. When Fs = 400 kHz and duty = 0.1, the minimum ESR is $\frac{T_{\rm on}}{2C_o}$ = 0.5 mΩ according to the critical condition given in [15]. However, the PM is less than 1° with the proposed loop gain analysis for such ESR. Therefore, the critical condition for ESR in [15] is insufficient to guarantee stability. With the optimum $R_c = \frac{T_{sw}}{\pi C_o}$ = 3.2 mΩ , the PM is close to 45° and the Fc is about half of Fs, which is compatible with previous analysis.

The load transition responses of RBCOT buck converter with different Rc are shown in Fig. 10. Smaller IL overshoot could be observed with larger Rc for better PM. The load transient recovery time is reduced with larger Rc since the Fc is increased with Rc according to previous analysis. It is proved that the correlation between loop gain properties (Fc and PM) and system stability for RBCOT control is the same as that of voltage-mode or current-mode control. Therefore, loop gain model can predict the transient response well for RBCOT control.

III. Modeling of Outer Integral Loop

The effect of the outer integral loop on the main regulation loop should be analyzed to guide its design. Assuming that the transconductance of the OTA in Fig. 11(a) is g_m, and its output resistance is $\rm R_{out}$, the transfer function from the difference between $V_{\rm out}$ and $V_{\rm ref}$ to V_c could be expressed as:

$$F_{dc}\ (s) = \frac{V_c\,(s)}{V_{\rm ref} - V_{\rm out}\,(s)} = \frac{g_m R_{\rm out}}{1 + sR_{\rm out}C_{\rm int}} \tag{15}$$

where $C_{\rm int}$ is the integral capacitance. The unit gain band width (UGBW) of $F_{\rm dc}$(s) is $g_m/C_{\rm int}$. Fig. 11(b) shows the proposed small signal model which includes the effect of outer integral loop. The loop gain of the proposed model from the broken point is

$$F_{\rm loop\_all}\ (s) = (1 + F_{\rm dc}\,(s))\ F_{\rm loop}\,(s)$$
$$\approx \frac{g_m R_{\rm out}\left(1 + \frac{sC_{\rm int}}{g_m}\right)}{1 + sR_{\rm out}C_{\rm int}} F_{\rm loop}\ (s) = \frac{A_{dc}\left(1 + \frac{s}{\omega_{zdc}}\right)}{\left(1 + \frac{s}{\omega_{pdc}}\right)} F_{\rm loop}\,(s) \tag{16}$$

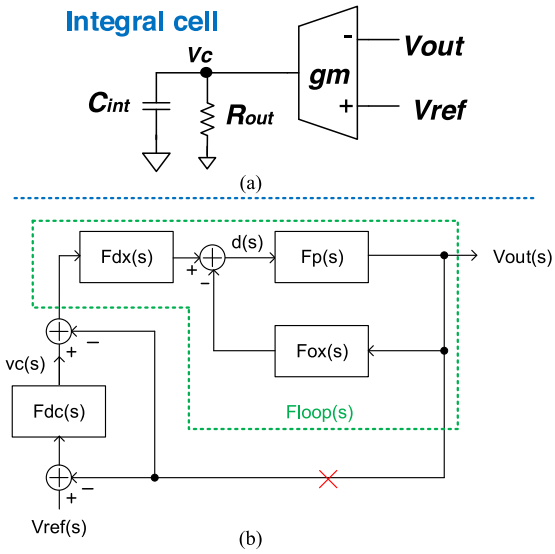

Fig. 11. (a) DC error integral block. (b)Small signal model with the outer integral loop.

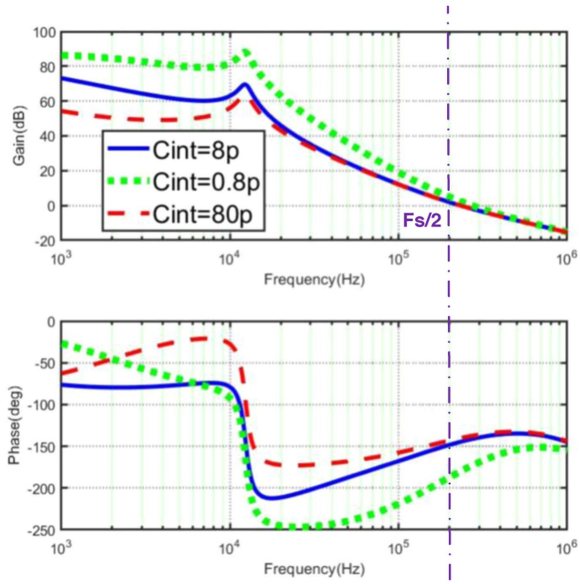

Fig. 12. Loop gain for different Cint ($V_{\rm in}$ = 12 V, $V_{\rm out}$ = 1.2 V, fs = 400 kHz, C = 250 μF, L = 660 nH, ESR = 3.2 mΩ, gm = 1 uS, and Rout = 100 MΩ).

where $A_{\rm dc}$ is the dc gain of the OTA and $F_{\rm loop}$(s) is the loop gain given in (12) without the outer integral loop. The pole-zero doublet $\omega_{zdc} = \frac{g_m}{C_{\rm int}}$ and $\omega_{pdc} = \frac{1}{R_{\rm out}C_{\rm int}}$ are generated by the outer integral loop. In order to make sure that ω_{zdc} and ω_{pdc} do not affect the system stability, the ω_{zdc} should be much less than the ω_c of the proposed loop gain model. Since the UGBW of Fdc(s) should meet the inequality as

$$\text{UGBW} = \frac{g_m}{C_{\rm int}} < \frac{\omega_{c\_\rm loop}}{10} \tag{17}$$

where $\omega_{c\_\rm loop}$ is the angular frequency of the system crossover frequency which is given in (13). The loop gain including the dc error integral block with different Cint is illustrated in Fig. 12, which shows the influence of the UGBW of $F_{\rm dc}$(s). Since the

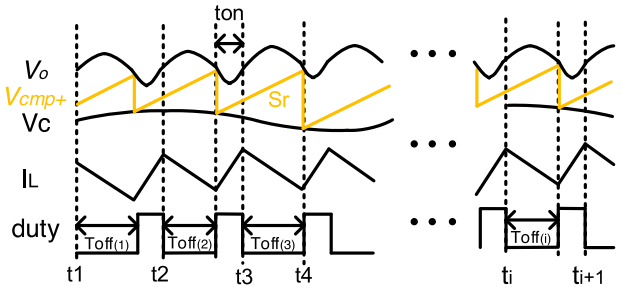

Fig. 13. Waveforms with V_c perturbation with the fixed slope ramp compensation.

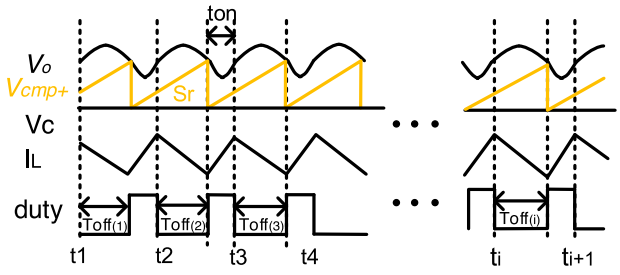

Fig. 14. Waveforms with V_o perturbation with the fixed slope ramp compensation.

internal loop $\mathrm{Fc_{loop}}$ is close to fs/2, the maximum UGBW of F_{dc}(s) is fs/20 = 20 kHz. When gm = 1 uS, the minimum C_{int} without deteriorating PM significantly is about 8 pF. A smaller C_{int} will make the system unstable, so (17) could be a design-oriented guidance for the dc error integral block.

IV. Extension to External Ramp Compensation

The proposed model strategy can be extended to external ramp compensation structures, including the fixed slope ramp compensation and the IL ac ramp compensation with an SW filter. Detailed analyses for these two compensation methods are presented in this section. ESR is neglected when ramp compensations are applied to simplify the modeling process.

A. Fixed Slope Ramp Compensation

Following the same modeling methodology, the perturbation $r_0 + \hat{r}\sin(\omega_m t - \theta)$ is added to the EA's output *Vc* while the V_{out} perturbation is neglected first. Based on the duty cycle and the output voltage waveforms in Fig. 13, it is found that

$$\begin{aligned} & v_c\left(t_{i-1}+T_{\mathrm{off}(i-1)}\right)+s_r\left(T_{\mathrm{on}}+T_{\mathrm{off}(i-1)}\right) \\ & \quad + \frac{\int_{t_{i-1}+T_{\mathrm{off}(i-1)}}^{t_i+T_{\mathrm{off}(i)}}\left(i_L(t)-\frac{v_o(t)}{R_L}\right)dt}{C_o} \\ & = v_c\left(t_i+T_{\mathrm{off}(i)}\right)+s_r\left(T_{on}+T_{\mathrm{off}(i)}\right) \end{aligned} \tag{18}$$

where S_r is the rising slope of the fixed slope ramp. Based on (18) and the steady-state relationship between V_{out} and IL, we can get

$$\begin{aligned} & \Delta T_{\mathrm{off}(i)}\left(s_r+\frac{s_{fl}T_{\mathrm{off}}}{2C_o}\right)-\Delta T_{off(i-1)}\left(2s_r\right. \\ & \quad \left.+\frac{s_{fl}\left(T_{\mathrm{off}}-2T_{sw}\right)}{2C_o}\right)+s_r\Delta T_{\mathrm{off}(i-2)} \\ & = v_c\left(t_{i-1}+T_{\mathrm{off}(i-1)}\right)-v_c\left(t_i+T_{\mathrm{off}(i)}\right) \\ & \quad -\left(v_c\left(t_{i-2}+T_{\mathrm{off}(i-2)}\right)-v_c\left(t_{i-1}+T_{\mathrm{off}(i-1)}\right)\right) \end{aligned} \tag{19}$$

where $S_{fl} = V\mathrm{out}/L$ is the falling slope of the inductor current. A Fourier analysis can be performed on the duty cycle and the DF from the output voltage to $d(s)$ can be calculated as

$$F_{dx\_s}(s) = \frac{f_s\left(1-e^{-j\omega_m T_{\mathrm{on}}}\right)\left(1-e^{-j\omega_m T_{sw}}\right)}{\left(s_r+\frac{s_{fl}T_{\mathrm{off}}}{2C_o}\right)-e^{-j\omega_m T_{sw}}\left(2s_r+\frac{s_{fl}\left(T_{\mathrm{off}}-2T_{sw}\right)}{2C_o}\right)+s_r e^{-2j\omega_m T_{sw}}}. \tag{20}$$

Then, the perturbation $r_0 + \hat{r}\sin(\omega_m t - \theta)$ is added to the output voltage $V_o(t)$ and the V_c perturbation is neglected. Based on the duty cycle and the output voltage waveforms in Fig. 14, it is found that

$$s_r\left(\Delta T_{\mathrm{off}(i)}-\Delta T_{\mathrm{off}(i-1)}\right)=\frac{\int_{t_{i-1}+T_{\mathrm{off}(i-1)}}^{t_i+T_{\mathrm{off}(i)}}\left(i_L(t)-\frac{V_0+v_o(t)}{R_L}\right)dt}{C_o}. \tag{21}$$

Based on (21) and the steady-state relationship between V_{out} and IL, one can get (22), shown at the bottom of the next page. A Fourier analysis can be performed on the duty cycle again and the DF from the output voltage to d(s) can be calculated as

$$F_{odx\_s}(s) = \frac{f_s\left(1-e^{-j\omega_m T_{\mathrm{on}}}\right)\left(1-e^{-j\omega_m T_{sw}}\right)\left[\frac{1}{(j\omega_m)^2 L C_o}+\frac{\frac{1}{R_L C_o}}{j\omega_m}\right]}{\left(s_r+\frac{s_f T_{\mathrm{off}}}{2C_o}\right)-e^{-j\omega_m T_{sw}}\left(2s_r+\frac{s_f\left(T_{off}-2T_{sw}\right)}{2C_o}\right)+s_r e^{-2j\omega_m T_{sw}}}. \tag{23}$$

The small signal model is the same as that shown in Fig. 7 and the transfer function is the same as (11) except the Rc is zero for $F_p(s)$. According to (9), (20), and (23), F_{loop}(s) can be simplified with the Padé Approximants as following:

$$F_{\mathrm{loop\_}s}(s) = \frac{A_{0\_s}\left(1+\frac{s}{Q_{zs}\omega_{zs}}+\frac{s^2}{\omega_{zs}^2}\right)}{\left(1+\frac{s}{Q_{ps2}\omega_{ps2}}+\frac{s^2}{\omega_{ps2}^2}\right)\left(1+\frac{s}{Q_{ps1}\omega_{ps1}}+\frac{s^2}{\omega_{ps1}^2}\right)} \tag{24}$$

where

$$\begin{aligned} A_x &= \left(\frac{T_{sw}}{\pi}\right)^2+\left(\frac{T_{\mathrm{on}}}{\pi}\right)^2-\left(\frac{T_{\mathrm{on}}}{2}\right)^2 \\ A_{0\_s} &= LC_o/\left[A_x+S_r T_{sw} C_o L/v_{\mathrm{out}}\right] \\ \omega_{zs} &= \pi/T_{sw} \\ Q_{zs} &= 2/\pi \end{aligned}$$

$$\omega_{ps1} = 1/\sqrt{LC_o}$$

$$Q_{ps1} = R_L\sqrt{C_o/L}$$

$$\omega_{ps2} = \pi\sqrt{A_x + \frac{S_r T_{sw} C_o L}{v_{\text{out}}}}\Big/\sqrt{T_{sw}^2 \times A_x + T_{\text{on}}^2 \frac{S_r T_{sw} C_o L}{v_{out}}}$$

$$Q_{ps2} \approx \sqrt{(T_{sw}^2 \times A_x + T_{\text{on}}^2 \frac{S_r T_{sw} C_o L}{v_{\text{out}}})(A_x + \frac{S_r T_{sw} C_o L}{v_{\text{out}}})}/\pi/\left(\frac{T_{sw}}{2}A_x + \frac{T_{\text{on}}}{2}\frac{S_r T_{sw} C_o L}{v_{\text{out}}}\right).$$

The double zero ω_{zs} is fixed to half of switching frequency and the double pole ω_{ps1} is generated of power stage. ω_{ps2} is higher than $\omega_{sw}/2$ and will be pushed to $\omega_{sw}/2$ when the duty cycle is close to 1. Assuming that ω_{zs} and ω_{ps2} do not affect the Fc significantly, the angular frequency of the Fc of $F_{\text{loop}}{}_s(s)$ can be expressed as

$$\omega_{c\_s} \approx \sqrt{A_{0\_s}}\,\omega_{ps1} = \frac{1}{\sqrt{\left(\frac{T_{sw}}{\pi}\right)^2 + \left(\frac{T_{\text{on}}}{\pi}\right)^2 - \left(\frac{T_{\text{on}}}{2}\right)^2 + \frac{V_{\text{slope}} C_o L}{v_{\text{out}}}}} < \frac{\pi}{T_{sw}} \quad (25)$$

where V_{slope} is the amplitude of the slope ramp in one cycle which can be expressed as $S_r \times T_{\text{sw}}$. The previous assumption is reasonable since the ω_{c_s} is less than ω_{zs} and ω_{ps2} , and ω_{c_s} will decrease when V_{slope} increasing. Considering the phase shift of ω_{zs} and ω_{ps2} at ω_{c_s}, the PM of $F_{\text{loop}}{}_s(s)$ can be expressed as

$$\text{PM}_s = \arctan\left(\frac{GBW_s/\omega_{zs}/Q_{zs}}{1-(GBW_s/\omega_{zs})^2}\right) - \arctan\left(\frac{GBW_s/\omega_{ps2}/Q_{ps2}}{1-(GBW_s/\omega_{ps2})^2}\right). \quad (26)$$

As shown in Fig. 15, too small V_{slope} will push ω_{ps2} and the Fc to *fs*/2 and make the system unstable, while too large V_{slope} will push the Fc to low frequency and the phase lift by ω_{zs} is attenuated. Thus, the control system will change to voltage mode without compensation with large V_{slope}, so the system will also be unstable. Therefore, an optimized V_{slope} could be obtained by searching the maximum value of (26). If the duty cycle is much less than 100%, the optimized slope could be expressed as

$$V_{\text{slope\_best}} = 2.3\frac{T_{sw}^2 V_{\text{out}}}{\pi^2 LC}. \quad (27)$$

With the optimized V_{slope}, the best PM is 35° and the Fc is close to $\frac{\pi}{2T_{sw}}$ according to (25) and (26). Therefore, PM is poor if

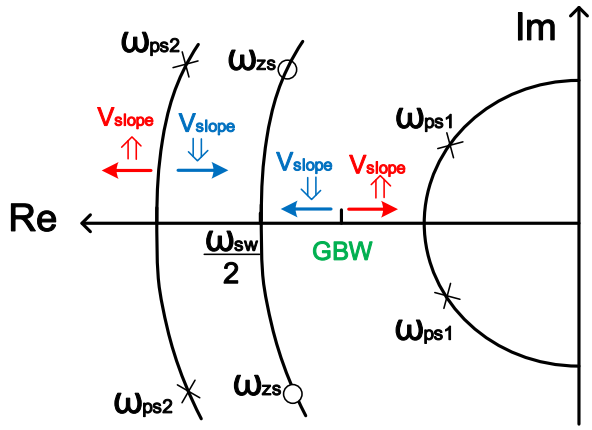

Fig. 15. Root locus diagram of the loop transfer function with the fixed slope ramp compensation.

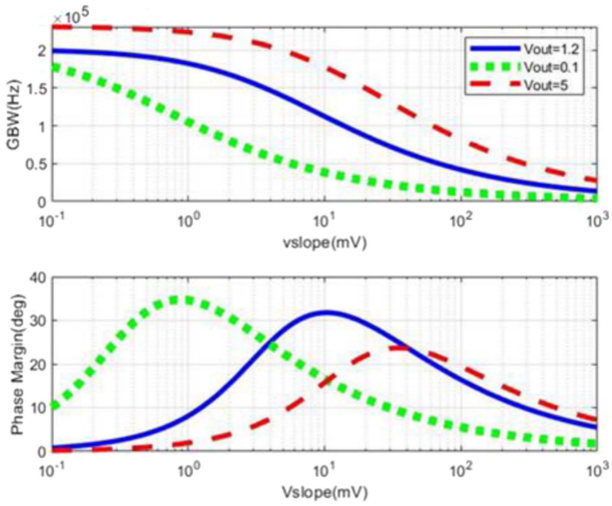

Fig. 16. Fc and PM versus V_{slope} in different Duty.

only the fixed slope ramp compensation is applied, which leads to oscillatory load transient performance with any slope value of the compensation ramp [2]. When $V_{\text{in}} = 12$ V, fs = 400 kHz, C = 250 μF, $L = 660$ nH, the relationship between V_{slope} and PM is plotted in Fig. 16 for different V_{out}. It is found the Fc will decrease with V_{slope} increasing and the optimized V_{slope} exists for different duty cycles according to PM curves. The best PM is 35° when duty cycle is smaller as previously analyzed and it will decrease when duty increases, which means the fixed slope

$$\begin{aligned} & s_r\left(\Delta T_{off(i)} - \Delta T_{off(i-1)}\right) - s_r\left(\Delta T_{off(i-1)} - \Delta T_{off(i-2)}\right) \\ &= \frac{v_0\left(t_i + T_{off(i)} + \frac{\pi}{2\omega_m}\right) - v_0\left(t_{i-1} + T_{off(i-1)} + \frac{\pi}{2\omega_m}\right) - v_0\left(t_{i-1} + T_{off(i-1)} + \frac{\pi}{2\omega_m}\right) - v_0\left(t_{i-2} + T_{off(i-2)} + \frac{\pi}{2\omega_m}\right)}{R_L C_o \omega_m} \\ &- \frac{s_{fl} T_{off}}{2C_o}\Delta T_{off(i)} - \frac{s_{fl}}{C_o} T_{sw}\Delta T_{off(i-1)} + \frac{s_{fl} T_{off}}{2C_o}\Delta T_{off(i-1)} \\ &- \frac{v_0\left(t_i + T_{off(i)} + \frac{\pi}{\omega_m}\right) - v_0\left(t_{i-1} + T_{off(i-1)} + \frac{\pi}{\omega_m}\right) - \left(v_0\left(t_{i-1} + T_{off(i-1)} + \frac{\pi}{\omega_m}\right) - v_0\left(t_{i-2} + T_{off(i-2)} + \frac{\pi}{\omega_m}\right)\right)}{\omega_m^2 LC_o} \end{aligned} \quad (22)$$

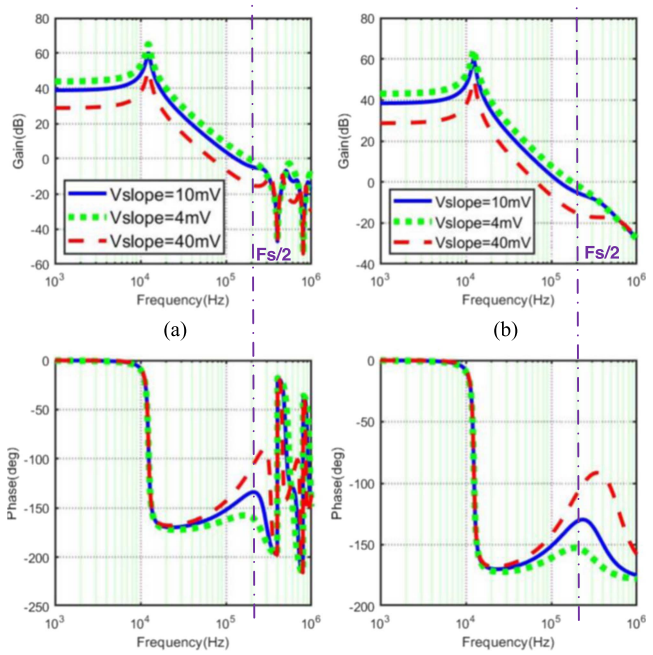

Fig. 17. Loop gain for different V_{slope} ($V_{\text{in}} = 12$ V, $V_{\text{out}} = 1.2$ V, fs = 400 kHz, C = 250 μF, and $L = 660$ nH). (a) Without approximants. (b) With approximants.

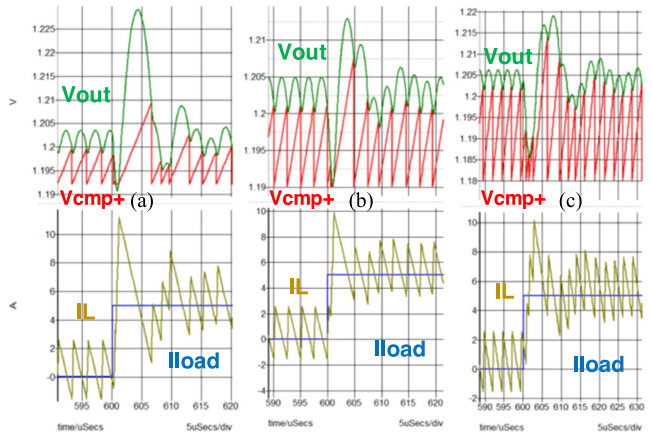

Fig. 18. Load transition for different V_{slope} ($V_{\text{in}} = 12$ V, $V_{\text{out}} = 1.2$ V, fs = 400 kHz, $C = 250$ μF, and $L = 660$ nH). (a) $V_{\text{slope}} = 6.8$ mV. (b) $V_{\text{slope}} = 10$ mV. (c) $V_{\text{slope}} = 20$ mV.

ramp compensation could not guarantee the loop stability when duty cycle is close to 1.

The bode diagrams of the proposed loop gain model with different slope ramps are shown in Fig. 17. When Fs = 400 kHz and duty = 0.1, according to the optimized slope amplitude in (27), the optimized V_{slope} is about 10 mV. With optimized V_{slope}, the PM is close to 35° and the Fc is about 1/4 of Fs, which is compatible with the analysis above.

The load transition responses of RBCOT buck converter with different V_{slope} are shown in Fig. 18. Compared with the recommended external ramp in [2] which is about 6.8 mV ($V_{\text{slope}} = \frac{1.21 \times T_{sw}^2 V_{\text{out}}}{8LC}$) when Fs = 400 kHz, duty = 0.1 and

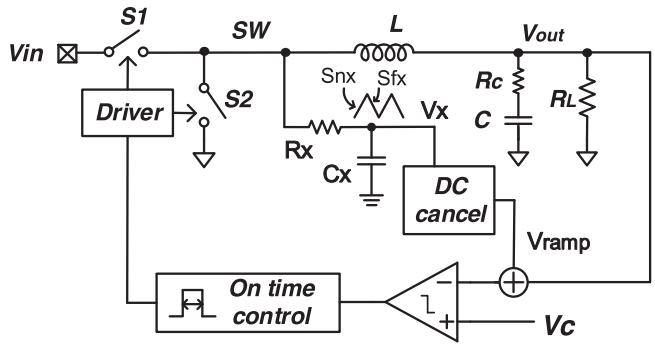

Fig. 19. RBCOT control with the SW filter ramp compensation.

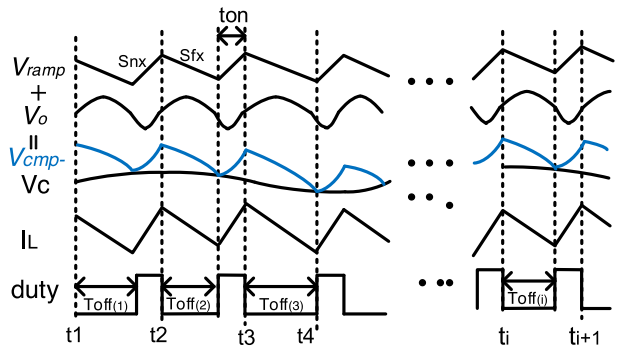

Fig. 20. Waveforms with V_c perturbation with the SW filter ramp.

Rc = 0, the smaller V_{out} overshoot and more stable IL transient waveform could be observed with proposed optimized V_{slope} which is 10 mV. Therefore, the loop gain model can achieve more accurate design guidance and analysis than conventional control to output transfer function.

B. IL AC Ramp Compensation With SW Filter

As shown in Fig. 19, *Rx* and *Cx* are used to generate the IL AC ramp compensation to exemplify the proposed modeling approach. The rising and falling slope of V_x could be expressed as $s_{nx} = \frac{V_{in} - V_x}{R_x C_x}$ and $s_{fx} = \frac{V_x}{R_x C_x}$, respectively. The dc value of V_x is the same as V_{out} and it could be cancelled to generate a ramp signal V_{ramp}. Following the same modeling methodology as above, a the perturbation $r_0 + \hat{r}\sin(\omega_m t - \theta)$ is added to the EA's output Vc while the V_{out} and V_x perturbations are neglected first.

Based on the duty cycle and the output voltage waveforms in Fig. 20, it is found that

$$v_c\left(t_{i-1} + T_{\text{off}(i-1)}\right) + s_{nx}T_{\text{on}} - s_{fx}T_{\text{off}(i)} + \frac{\int_{t_{i-1}+T_{\text{off}(i-1)}}^{t_i+T_{\text{off}(i)}} \left(i_L(t) - \frac{v_o(t)}{R_L}\right) dt}{C_o} = v_c\left(t_i + T_{\text{off}(i)}\right). \tag{28}$$

Based on (28) and the steady-state relationship between V_{out} and IL, we can get

$$\Delta T_{\text{off}(i)}\left(s_{fx} + \frac{s_{fl}T_{\text{off}}}{2C_o}\right) - \Delta T_{\text{off}(i-1)}\left(s_{fx} + \frac{s_{fl}\left(T_{off} - 2T_{sw}\right)}{2C_o}\right)$$

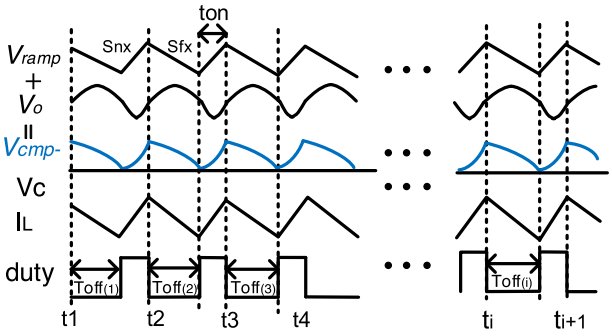

Fig. 21. Waveforms with V_o perturbation with the SW filter ramp.

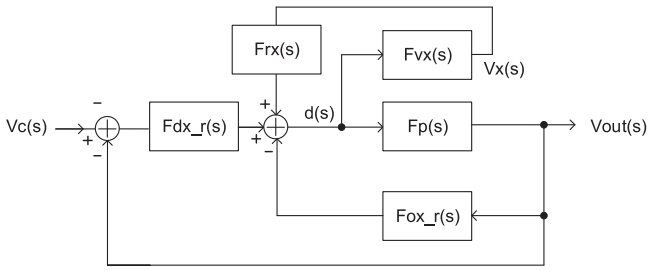

Fig. 22. Small signal model for the RBCOT controlled buck converter with the SW filter ramp.

$$= v_c\left(t_{i-1}+T_{\text{off}(i-1)}\right)-v_c\left(t_i+T_{\text{off}(i)}\right) \quad (29)$$
$$-\left(v_c\left(t_{i-2}+T_{\text{off}(i-2)}\right)-v_c\left(t_{i-1}+T_{\text{off}(i-1)}\right)\right)$$

where $S_{fl} = V\text{out}/L$ is the falling slope of inductor current. A Fourier analysis is performed on the duty cycle and the DF from the output voltage to $d(s)$ can be calculated as

$$F_{dx\_r}(s) = \frac{f_s\left(1-e^{-j\omega_m T_{\text{on}}}\right)\left(1-e^{-j\omega_m T_{sw}}\right)}{\left(s_{fx}+\frac{s_{fl}T_{\text{off}}}{2C_o}\right)-e^{-j\omega_m T_{sw}}\left(s_{fx}+\frac{s_{fl}(T_{\text{off}}-2T_{sw})}{2C_o}\right)}. \quad (30)$$

Then, the perturbation $r_0+\hat{r}\sin(\omega_m t-\theta)$ is added to output voltage $V_o(t)$, and the V_c and V_x perturbations are neglected. Based on the duty cycle and the output voltage waveforms in Fig. 21, it is found that

$$s_{nx}T_{\text{on}}-s_{fx}T_{\text{off}(i)}++\frac{\int_{t_{i-1}+T_{\text{off}(i-1)}}^{t_i+T_{\text{off}(i)}}\left(i_L(t)-\frac{v_o(t)}{R_L}\right)dt}{C_o}=0 \quad (31)$$

Based on (31) and the steady-state relationship between V_{out} and IL, one can get expression (32) shown at the bottom of this page. A Fourier analysis is performed on the duty cycle again and the DF from the output voltage to $d(s)$ can be calculated as

$$F_{odx\_r}(s) = \frac{f_s\left(1-e^{-j\omega_m T_{\text{on}}}\right)\left(1-e^{-j\omega_m T_{sw}}\right)\left[\frac{1}{(j\omega_m)^2 LC_o}+\frac{\frac{1}{R_L C_o}}{j\omega_m}\right]}{\left(s_{fx}+\frac{s_{fl}T_{\text{off}}}{2C_o}\right)-e^{-j\omega_m T_{sw}}\left(s_{fx}+\frac{s_{fl}(T_{\text{off}}-2T_{sw})}{2C_o}\right)}. \quad (33)$$

Finally, V_{out} and V_c perturbations are neglected and we only consider the influence of the V_x perturbation to S_{nx} and S_{fx}. When the perturbation $r_0+\hat{r}\sin(\omega_m t-\theta)$ is added to V_x, the duty cycle and the output voltage waveforms are the same as those in Fig. 20. It is found that

$$s_{nx}T_{\text{on}}-s_{fx}T_{\text{off}(i)}+\frac{\int_{t_{i-1}+T_{\text{off}(i-1)}}^{t_i+T_{\text{off}(i)}}\left(i_L(t)-\frac{v_o(t)}{R_L}\right)dt}{C_o}=0. \quad (34)$$

Based on (34) and the steady-state relationship between V_{out} and IL, we can get

$$T_{\text{off}(i)}\left(s_{fx}+s_{fl}\frac{T_{off}}{2C_o}\right)-\Delta T_{\text{off}(i-1)}\left(s_{fx}+s_{fl}\frac{T_{\text{off}}-2T_{sw}}{2C_o}\right)$$
$$=\frac{1}{\frac{R_x C_x}{\omega_m}}\left(\hat{v}_x\left(t_i+T_{\text{off}(i)}+\frac{\pi}{2\omega_m}\right)-\hat{v}_x\left(t_{i-1}+T_{\text{off}(i-1)}+\frac{\pi}{2\omega_m}\right)\right). \quad (35)$$

The similar Fourier analysis is performed on the duty cycle again and the DF from the V_x to $d(s)$ can be calculated as

$$F_{rx}(s) = \frac{d(s)}{v_x(s)}$$
$$= \frac{f_s\left(1-e^{-j\omega_m T_{\text{on}}}\right)\left(1-e^{-j\omega_m T_{sw}}\right)\times\frac{\frac{1}{R_x C_x}}{j\omega_m}}{\left(s_{fx}+\frac{s_{fl}T_{\text{off}}}{2C_o}\right)-e^{-j\omega_m T_{sw}}\left(s_{fx}+\frac{s_f(T_{\text{off}}-2T_{sw})}{2C_o}\right)}. \quad (36)$$

Then, the loop model for RBCOT buck converter with SW filter ramp compensation is shown as Fig. 22. Compared to previous loop model in Fig. 7, one more internal loop is included which is contributed by V_x. $F_{vx}(s)$ is the transfer function from the duty cycle to V_x. According to the V_x generator in Fig. 16, it could be expressed as

$$F_{vx}(s) = \frac{V_{\text{in}}}{1+sR_x C_x}. \quad (37)$$

$$\Delta T_{\text{off}(i)}\left(s_{fx}+s_{fl}\frac{T_{\text{off}}}{2C_o}\right)-\Delta T_{\text{off}(i-1)}\left(s_{fx}+s_{fl}\frac{T_{off}-2T_{sw}}{2C_o}\right)=\frac{\frac{1}{R_L C_o}}{\omega_m}\left(\hat{v}_o\left(t_i+T_{off(i)}+\frac{\pi}{2\omega_m}\right)\right.$$
$$\left.-\hat{v}_o\left(t_{i-1}+T_{off(i-1)}+\frac{\pi}{2\omega_m}\right)-\left(\hat{v}_o\left(t_{i-1}+T_{off(i-1)}+\frac{\pi}{2\omega_m}\right)-\hat{v}_o\left(t_{i-2}+T_{off(i-2)}+\frac{\pi}{2\omega_m}\right)\right)\right)$$
$$+\frac{\left(\hat{v}_o\left(t_i+T_{off(i)}\right)-\hat{v}_o\left(t_{i-1}+T_{off(i-1)}\right)\right)-\left(\hat{v}_o\left(t_{i-1}+T_{\text{off}(i-1)}\right)-\hat{v}_o\left(t_{i-2}+T_{\text{off}(i-2)}\right)\right)}{\omega_m^2 LC_o}. \quad (32)$$

Therefore, the loop gain for the model in Fig. 22 is

$$F_{\text{loop\_}r}(s) = \frac{F_{dx\_r}(s) \times F_p(s)}{1 + F_{ox\_r}(s) \times F_p(s) - F_{rx}(s) \times F_{vx}(s)}. \tag{38}$$

According to (9), (29), (32), and (35), $F_{\text{loop}}(s)$ can be simplified with the Padé Approximants as

$$F_{\text{loop\_}r}(s) = \frac{A_{0\_r}\left(1 + \frac{s}{\omega_{zr}}\right)}{\left(1 + \frac{s}{Q_{pr1}\omega_{pr1}} + \frac{s^2}{\omega_{pr1}^2}\right)\left(1 + \frac{s}{Q_{pr2}\omega_{pr2}} + \frac{s^2}{\omega_{pr2}^2}\right)} \tag{39}$$

where

$$\begin{aligned}
A_{xr} &= \left(\frac{T_{sw}}{\pi}\right)^2 + \left(\frac{T_{\text{on}}}{\pi}\right)^2 + \left(\frac{LC_o}{R_xC_x} - \frac{T_{\text{on}}}{2}\right)\frac{T_{\text{on}}}{2} \\
B_{xr} &= \left(\frac{T_{\text{on}}}{\pi}\right)^2 \left(\frac{LC_o}{R_xC_x} - \frac{T_{\text{on}}}{2}\right) + \frac{T_{\text{on}}T_{sw}^2}{2\pi^2} \\
A_{0_r} &= LC_o/\left[LC_o + A_x\right], \\
\omega_{zr} &= 1/R_xC_x, \\
\omega_{pr1} &= 1/\sqrt{LC_o}, \\
Q_{pr1} &= R_L\sqrt{C_o/L}, \\
\omega_{pr2} &= \sqrt{LC_o}/\sqrt{R_xC_xB_x}, \\
Q_{pr2} &= \sqrt{LC_oB_x}/\sqrt{R_xC_x}A_x.
\end{aligned}$$

The zero ω_{zr} is introduced by the SW filter R_x and C_x, and the double pole ω_{pr1} are generated by the power stage. ω_{pr2} is around *fs*/2 and will be pushed to a lower frequency when R_xC_x increases. Assuming that ω_{zr} is much lower than ω_c (the angular frequency of Fc) and ω_{pr2} will not affect the ω_c significantly, the ω_c and the PM of $F_{\text{loop}\cdot r}(s)$ can be expressed as

$$\omega_c \approx \frac{A_0\omega_{pr1}^2}{\omega_{zr}} = \frac{R_xC_x}{LC_o} \tag{40}$$

$$\begin{aligned}
\text{PM} &= 90^\circ - \arctan\left(\frac{\frac{\frac{Fc}{\omega_{p2}}}{Q_{p2}}}{1 - \left(\frac{Fc}{\omega_{p2}}\right)^2}\right) \\
&\approx \arctan\left(A_x\left(\frac{R_xC_x}{LC_o}\right)^2\right).
\end{aligned} \tag{41}$$

As shown in Fig. 23, too small V_{ramp} with large R_xC_x will push ω_{ps2} towards the ω_c and make the system unstable, while the ω_c will decrease and the system response becomes slow if V_{ramp} is too large with small R_xC_x. Therefore, optimized virtual IL ramp amplitude is required for the system.

In order to keep a relatively fast system response, the Fc should be higher than 1/10 of the switching frequency. According to (40), R_xC_x should satisfy the inequality as

$$R_xC_x > \frac{\pi LC_o}{5T_{sw}}. \tag{42}$$

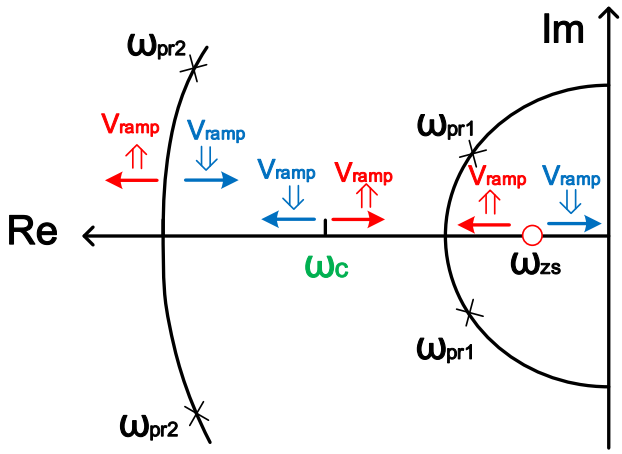

Fig. 23. Root locus diagram of the loop transfer function with SW filter ramp compensation.

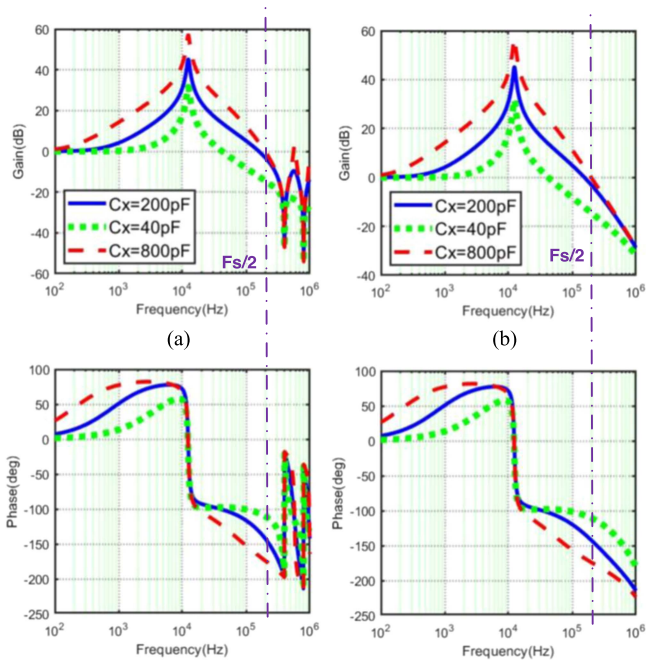

Fig. 24. loop gain for different V_{ramp} (V_{in} = 12 V, V_{out} = 1.2 V, fs = 400 kHz, C = 250 μF, L = 660 nH, and Rx = 1 MΩ). (a) Without approximants. (b) With approximants.

Assume that PM > 45° is necessary for stable operation, the maximum R_xC_x could be obtained from (40)

$$R_xC_x < \sqrt{\frac{\tan\left(90^\circ - PM_{\min}\right)}{A_x}}LC_o \tag{43}$$

Based on (42) and (43), the optimized range for R_xC_x can be concluded as follow:

$$\frac{\pi LC_o}{5T_{sw}} < R_xC_x < \frac{LC_o}{\sqrt{\left(\frac{T_{sw}}{\pi}\right)^2 + \left(\frac{T_{on}}{\pi}\right)^2}}. \tag{44}$$

The bode diagrams of the proposed loop gain model with different SW filters are shown in Fig. 24. These diagrams confirm that Padé Approximants could guarantee the modeling accuracy

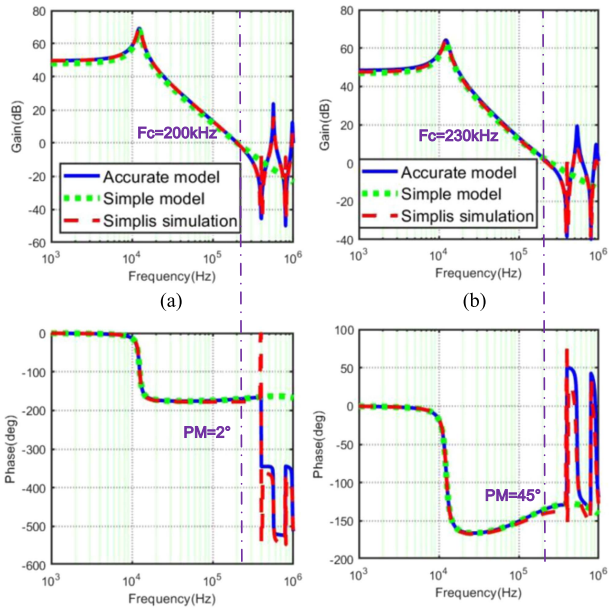

Fig. 25. Loop gain verification for the ESR ripple compensation. (a) $R_c = 1$ mΩ. (b) $R_c = 4$ mΩ.

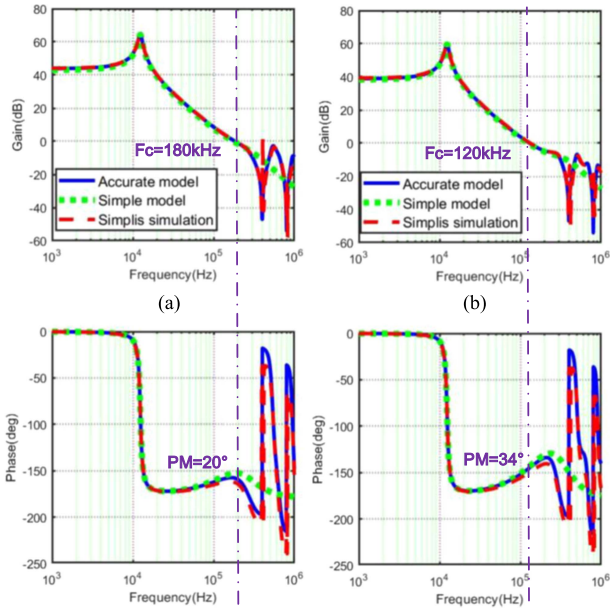

Fig. 26. Loop gain verification for fixed slope ramp compensation. (a) $V_{\rm slope} = 4$ mV. (b) $V_{\rm slope} = 10$ mV.

up to half of the switching frequency. When Fs = 400 kHz, duty = 0.1, and $Rx = 1$ MΩ, the optimum value for C_x is from 40 to 200 pF according to (44) The PM is close to 45° when C_x takes the upper limit and the Fc is about 40 kHz when C_x reaches the lower limit, which is compatible with above analysis. If $V_{\rm ramp}$ is less than the optimized value with 800 pF C_x, the PM is less than 10° and the stability could not be guaranteed.

V. Simulation and Experimental Verification

The SIMPLIS simulation tool has been extensively used to verify the proposed model for the RBCOT control. The parameters of the buck converter under verification are as follows: $V_{\rm in} = 12$ V; $V_{\rm out} = 1.2$ V; fs = 400 kHz; $C = 250$ μF; and $L = 660$ nH. The bode diagrams of the loop gain of the RBCOT controlled buck converter with the ESR ripple compensation are shown in Fig. 25. The accurate model is (11) without the Padé Approximants. The simple model is (12) after the Padé Approximants. It could be found the accurate model can accurately predict the system response even beyond the switching frequency. The accuracy of simple model is limited to below 1/2 fs, nevertheless the Fc and the PM match well with (13) and (14).

The two external ramp compensation approaches to guarantee the stability independent of the ESR in RBCOT controlled buck converter are also verified through SIMPLIS simulations. For the case of adding the fixed slope ramp compensation, the loop gain is shown in Fig. 26(a) and (b). The best PM lift is achieved with optimized $V_{\rm slope}$ according to (27). For the case of the IL ac ramp compensation with SW filter, the results are shown in Fig. 27(a) and (b). All these results show the validity of the proposed model even beyond the switching frequency, which is achieved by the proposed modeling approach.

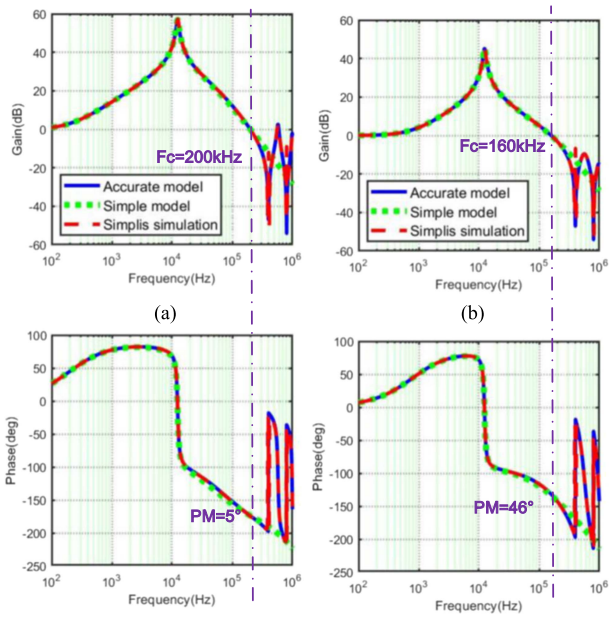

Fig. 27. Loop gain verification for the IL ac ramp compensation with the SW filter ($Rx = 1$ MΩ). (a) $C_x = 800$ pF. (b) $C_x = 200$ pF.

The proposed loop gain model is also verified by the hardware measurement results. A prototype of a constant on-time buck converter is built based on the controller MPQ8632 from Monolithic Power Systems. Fig. 28 shows the circuit diagram, and the detailed specifications are listed as follows: Vin = 12 V; Vout = 1.2 V; Fs = 600 kHz, L = 1 μH; and $RL = 0.4$ Ω. The ceramic capacitor C1206X5R226M350NT (22 μF/16 V) manufactured by SANYEAR is used as the output capacitor with 7 mΩ ESR according to datasheet. The actual capacitance of this capacitor is 14 μF considering the dc bias influence, which is measured according to output voltage ripple and IL ripple with following

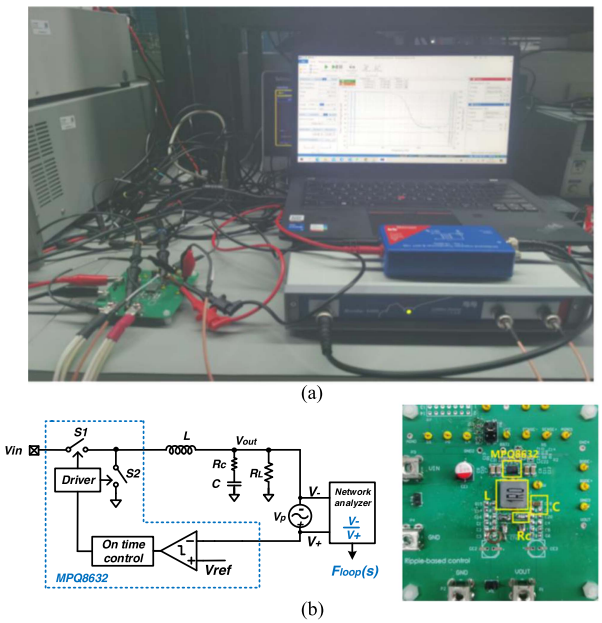

Fig. 28. (a) Experimental setup and (b) simplified diagram of prototype for experimental verification.

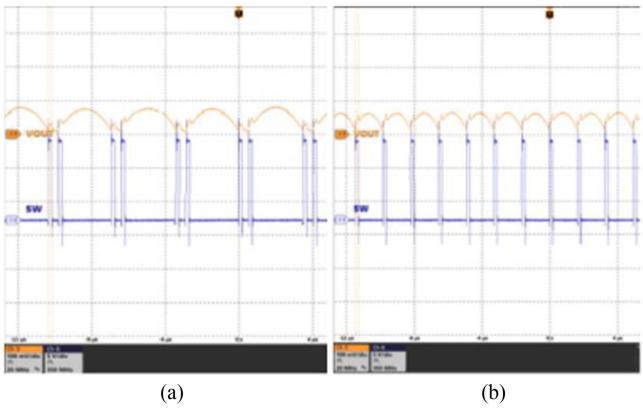

Fig. 29. Steady-state output voltage (*V*out) and switching node voltage (*V*sw). (a) Rc = 7 mΩ. (b) Rc = 22 mΩ.

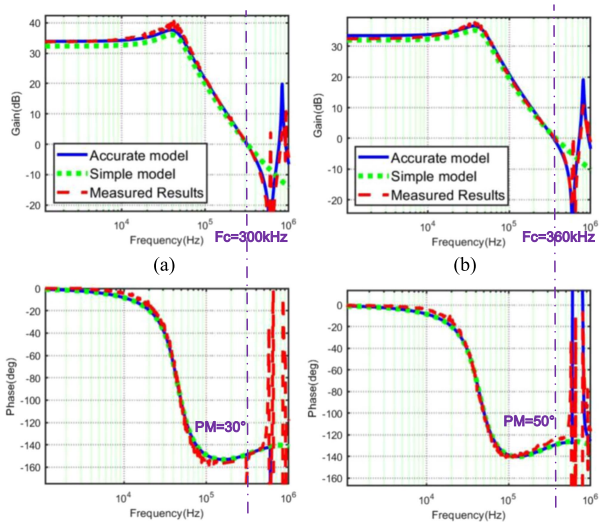

Fig. 30. Loop gain comparison (*C*out = 14 uF). (a) Rc = 22 mΩ. (b) Rc = 37 mΩ.

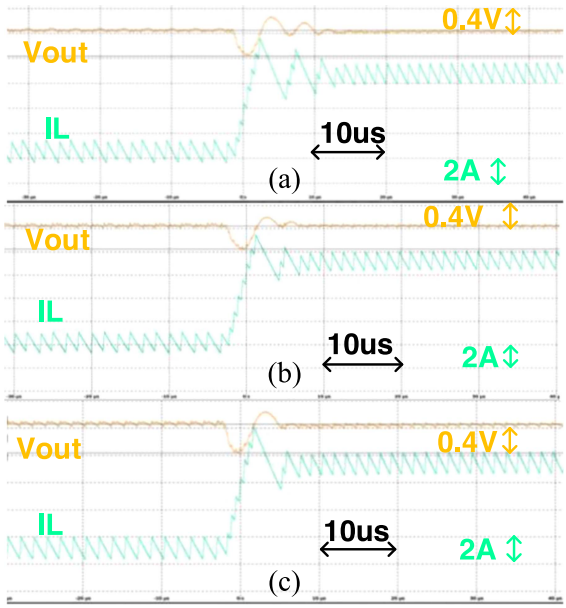

Fig. 31. Load transient response comparison. (a) Rc = 10 mΩ. (b) Rc = 22 mΩ. (c) Rc = 37 mΩ.

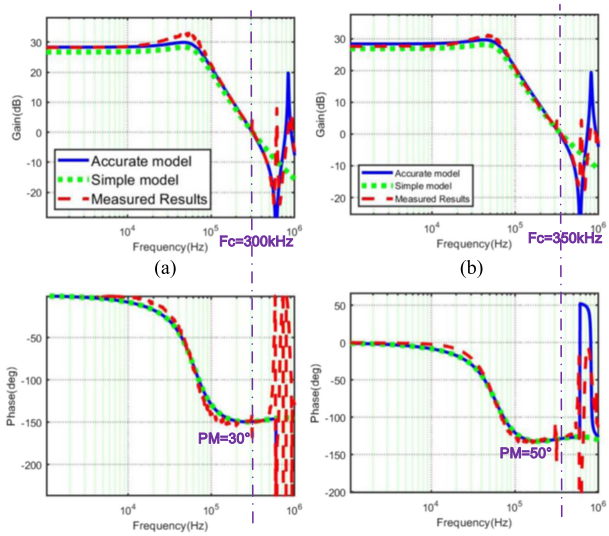

Fig. 32. Loop gain comparison (*C*out = 7 uF). (a) Rc = 40 mΩ. (b) Rc = 80 mΩ.

expression:

$$C_{\text{actual}} = \frac{\Delta I_L T_{sw}}{8\left(V_{\text{out\_ripple}} - \Delta I_L \text{ESR}\right)} \tag{45}$$

where ΔI_L and $V_{\text{out\_ripple}}$ are the IL ripple and output voltage ripple in one period, respectively.

The time-domain waveforms with different ESR are shown in Fig. 29. Subharmonic oscillations occur in case (a) even Rc is larger than the critical condition for ESR which is Ton/(2C). While, with the proposed loop gain model, the PM is less than 10° for this case.

The loop gain is measured by inserting a perturbation signal V_p into the feedback loop with the network analyzer OMICRON Lab Bode 100 as shown in Fig. 28(b). The loop gain transfer

function $F_{\text{loop}}(s)$ is the ratio of the returned signal $V-$ to the perturbation input signal $V+$. Transfer function measurements with different values for Rc are shown in Fig. 30. The proposed model can accurately predict the dc gain, Fc, PM and double pole of power stage. With the optimized $R_c = \frac{T_{sw}}{\pi C_o} = 37\,\text{m}\Omega$, the PM is about 50°, which agrees with the model results well.

Measured 6 A load transient waveforms with different values for Rc are shown in Fig. 31. Faster response speed and smaller IL overshoot could be observed with larger ESR, which is corresponding with Fc and PM results in loop gain model and measurement.

When the output capacitor is changed to GMK316BJ106KL-T (10 uF/35 V) manufactured by TAIYO with 7 uF actual measured capacitance according to (45), the modeling results could also match well with transfer function measurements as shown in Fig. 32.

VI. Conclusion

This article has presented a new modeling approach for the RBCOT control. By applying basic principle of the DF method, an loop gain model for the RBCOT control which is accurate even beyond the switching frequency is proposed. This model can accurately predict the relationship between stability and the ESR ripple with more details than previous works. Two types of the external ramp compensation schemes including the fixed slope ramp and the IL ac ramp with an SW filter are modeled and analyzed to solve the instability issue when the ESR is very small. The pole-zero movements of the loop gain models have been identified in both types of the external ramp compensation schemes and the best range of ramp compensation amplitudes are also given as a design guideline. SIMPLIS simulation and experimental results verify the proposed model.

References

[1] T. Qian and B. Lehman, "An adaptive ramp compensation scheme to improve stability for DC-DC converters with ripple-based constant on-time control," in *Proc. IEEE Energy Convers. Congr. Expo.*, 2014, pp. 3424–3428.

[2] S. Tian, F. C. Lee, P. Mattavelli, K. Cheng, and Y. Yan, "Small-signal analysis and optimal design of external ramp for constant on-time V^2 control with multilayer ceramic caps," *IEEE Trans. Power Electron.*, vol. 29, no. 8, pp. 4450–4460, Aug. 2014.

[3] Y. Yan, P. Liu, F. Lee, Q. Li, and S. Tian, "V_2 control with capacitor current ramp compensation using lossless capacitor current sensing," in *Proc. IEEE Energy Convers. Congr. Expo.*, 2013, pp. 117–124.

[4] S.-H. Pan, C.-J. Chen, and C.-J. Tsai, "A novel capacitor current constant on-time controlled buck converter at 4-mhz switching frequency," in *Proc. IEEE Energy Convers. Congr. Expo.*, 2018, pp. 6008–6013.

[5] J. J. Lu, C. Chen, C. Hong, and C. Tsai, "A novel ripple-coupling constant on-time controlled buck converter IC with highly digital charge-pump based error amplifier," in *Proc. IEEE Appl. Power Electron. Conf. Expo.*, 2019, pp. 1766–1769.

[6] Y.-C. Lin, C.-J. Chen, D. Chen, and B. Wang, "A novel ripple-based constant on-time control with virtual inductance and offset cancellation for DC power converters," in *Proc. IEEE Energy Convers. Congr. Expo.*, 2011, pp. 1244–1250.

[7] C.-J. Chen, D. Chen, C.-W. Tseng, C.-T. Tseng, Y.-W. Chang, and K. Wang, "A novel ripple-based constant on-time control with virtual inductor current ripple for buck converter with ceramic output capacitors," in *Proc. 26th Annu. IEEE Appl. Power Electron. Conf. Expo.*, 2011, pp. 1488–1493.

[8] I.-C. Wei, D. Chen, Y.-C. Lin, and C.-J. Chen, "The stability modeling of ripple-based constant on-time control schemes used in the converters operating in DCM," in *Proc. Int. Conf. Renew. Energy Res. Appl.*, 2012, pp. 1–8.

[9] S. Tian, K.-Y. Cheng, F. C. Lee, and P. Mattavelli, "Small-signal model analysis and design of constant-on-time V_2 control for low-ESR caps with external ramp compensation," in *Proc. IEEE Energy Convers. Congr. Expo.*, 2011, pp. 2944–2951.

[10] R. W. Erickson and D. Maksimovic, *Fundamentals Power Electron*, 2nd ed. Norwell, MA, USA: Kluwer, 2001.

[11] W. Huang, "A new control for multi-phase buck converter with fast transient response," in *Proc. 16th Annu. IEEE Appl. Power Electron. Conf. Expo.*, pp. 273–279, 2001.

[12] S. Qu, "Modeling and design considerations of V^2 controlled buck regulator," in *Proc. 16th Annu. IEEE Appl. Power Electron. Conf. Expo.*, 2001, pp. 507–513.

[13] R. Redl and J. Sun, "Ripple-based control of switching regulators—An overview," *IEEE Trans. Power Electron.*, vol. 24, no. 12, pp. 2669–2680, Dec. 2009.

[14] N. Yan, X. Ruan, and X. Li, "A general approach to sampled-data modeling for ripple-based control—Part II: Constant ON-time and constant OFF-time control," *IEEE Trans. Power Electron.*, vol. 37, no. 6, pp. 6385–6396, Jun. 2022.

[15] J. Sun, "Characterization and performance comparison of ripple-based control for voltage regulator modules," *IEEE Trans. Power Electron.*, vol. 21, no. 2, pp. 346–353, Mar. 2006.

[16] A. El Aroudi, B. Robert, and L. Martinez-Salamero, "Modelling and analysis of multicell converters using discrete time models," in *Proc. IEEE Int. Symp. Circuits Syst.*, 2006.

[17] X. Zhang, Z. Zhang, H. Bao, B. Bao, and X. Qu, "Stability effect of control weight on multiloop COT-controlled buck converter with PI compensator and small output capacitor ESR," *IEEE J. Emerg. Sel. Topics Power Electron.*, vol. 9, no. 4, pp. 4658–4667, Aug. 2021.

[18] J. Wang, B. Bao, J. Xu, G. Zhou, and W. Hu, "Dynamical effects of equivalent series resistance of output capacitor in constant on-time controlled buck converter," *IEEE Trans. Ind. Electron.*, vol. 60, no. 5, pp. 1759–1768, May 2013.

[19] F. Bizzarri, L. Gardini, P. Nora, and A. Brambilla, "A stability condition for constant-on time buck converters suitable for automotive applications," in *Proc. IEEE Int. Symp. Circuits Syst.*, 2021, pp. 1–5.

[20] J. Cortés, V. Šviković, P. Alou, J. A. Oliver, J. A. Cobos, and R. Wisniewski, "Accurate analysis of subharmonic oscillations of V^2 and V^2ic controls applied to buck converter," *IEEE Trans. Power Electron.*, vol. 30, no. 2, pp. 1005–1018, Feb. 2015.

[21] J. Li and F. C. Lee, "New modeling approach and equivalent circuit representation for current-mode control," *IEEE Trans. Power Electron.*, vol. 25, no. 5, pp. 1218–1230, May 2010.

[22] J. Li and F. C. Lee, "New modeling approach for current-mode control," in *Proc. 24th Annu. IEEE Appl. Power Electron. Conf. Expo.*, 2009, pp. 305–311.

[23] S. Tian, F. C. Lee, J. Li, Q. Li, and P.-H. Liu, "A three-terminal switch model of constant on-time current mode with external ramp compensation," *IEEE Trans. Power Electron.*, vol. 31, no. 10, pp. 7311–7319, Oct. 2016.

[24] J. Li and F. C. Lee, "Modeling of V^2 current-mode control," *IEEE Trans. Circuits Syst. I, Reg. Papers*, vol. 57, no. 9, pp. 2552–2563, Sep. 2010.

[25] Y. Yan, F. C. Lee, S. Tian, and P.-H. Liu, "Modeling and design optimization of capacitor current ramp compensated constant on-time V^2 control," *IEEE Trans. Power Electron.*, vol. 33, no. 8, pp. 7288–7296, Aug. 2018.

[26] B. Wang, D. Chen, C.-J. Chen, and S.-F. Hsiao, "Stability prediction of integrated-circuit based constant ON-time controlled buck converters," *IEEE Trans. Power Electron.*, vol. 36, no. 6, pp. 6838–6849, Jun. 2021.

[27] R. B. Ridley, B. H. Cho, and F. C. Y. Lee, "Analysis and interpretation of loop gains of multiloop-controlled switching regulators (power supply circuits)," *IEEE Trans. Power Electron.*, vol. 3, no. 4, pp. 489–498, Oct. 1988.

[28] F. Yu and F. C. Lee, "Design oriented model for constant on-time V_2 control," in *Proc. IEEE Energy Convers. Congr. Expo.*, 2010, pp. 3115–3122.

[29] Y. Yan, F. C. Lee, P. Mattavelli, and S. Tian, "Small signal analysis of V^2 control using equivalent circuit model of current mode controls," *IEEE Trans. Power Electron.*, vol. 31, no. 7, pp. 5344–5353, Jul. 2016.

[30] S. Tian, F. C. Lee, Q. Li, and Y. Yan, "Unified equivalent circuit model and optimal design of V^2 controlled buck converters," *IEEE Trans. Power Electron.*, vol. 31, no. 2, pp. 1734–1744, Feb. 2016.

[31] X. Lou, Q. Li, F. C. Lee, and M. H. Ahmed, "Modeling and analysis of current mode and V^2 controls with adaptive voltage positioning (AVP) design," in *Proc. IEEE Appl. Power Electron. Conf. Expo.*, 2021, pp. 2549–2555.

[32] G. A. Baker and P. Graves-Morris, *Padé Approximants*. New York, NY, USA: Cambridge Univ. Press, 1996.

Danzhu Lu (Senior Member, IEEE) received the B.S. and M.S. degrees in microelectronics in 2010 and 2013, respectively, from the State Key Laboratory of ASIC and System in Fudan University, Shanghai, China, where he is currently working toward the Ph.D. degree in electronic information with the State Key Laboratory of Integrated Chips and Systems, School of Microelectronics.

He was an Analog Design Engineer with Analog Device Inc. in Shanghai site, from 2013 to 2020. After that, he has been the Analog IC Design Director with Bright Power Semiconductor, since 2020. His current research interests include design and modeling of power management systems, especially ultra-low power converters and COT controlled power converters.

Xiaoyang Zeng (Senior Member, IEEE) received the B.Sc. degree from Xiangtan University, Xiangtan, China, in 1996, and the Ph.D. degree (Hons.) from the Changchun Institute of Optics, Fine Mechanics and Physics, Chinese Academy of Sciences, Beijing, China, in 2001.

From March 2001 to February 2003, he was a Post-Doctoral Researcher with Fudan University, Shanghai, China, where he has been a Faculty Member since 2003 and the Chair Professor and Executing Director of the State Key Laboratory of Integrated Chips and Systems. He has authored or coauthored more than 200 articles in international journals and conferences, such as the IEEE International Solid-State Circuits Conference, IEEE JOURNAL OF SOLID-STATE CIRCUITS, IEEE TRANSACTIONS ON CIRCUITS AND SYSTEMS, IEEE TRANSACTIONS ON VERY LARGE SCALE INTEGRATION SYSTEMS, IEEE VLSI Symposia, the IEEE CICC, IEEE ESSCIRC, IEEE ASP-DAC, and the IEEE A-SSCC, and applied for more than 120 patents. His research fields include information security chips, baseband processing technologies for wireless communication, and mixed-signal IC designs and ultralow power IC methodology.

Dr. Zeng is also the Chair of the Shanghai Chapter of the IEEE SSCS, a TPC Member of the ISSCC, the Co-Chair of the Circuit and System Division of the Chinese Institute of Electronics, a member of the Steering Committee of ASPDAC and the A-SSCC Technical Committee, and the TPC Chair of ASICON 2009 and 2013. He was the recipient of the National Science Fund for Distinguished Young Scholars in 2015, the Award of Distinguished Professor of Yangtze River Scholar in 2016, and also the Award of the Science and Technology Innovation Youth Leader of the Ministry of Science and Technology in 2017. He was also the recipient of Award of Top Ten New IT Youth in Shanghai in 2009, the Award of Twilight Scholar in Shanghai in 2011, and the Award of Excellent Academic Leaders in Shanghai in 2015.

Zhiliang Hong (Senior Member, IEEE) received the B.S. degrees from the University of Science and Technology of China, Hefei, China, and the Ph.D. degree from the Swiss Federal Institute of Technology (ETHZ), Zurich, Switzerland.

He was the Leader of the Chinese Delegation in co-operation design with Venus System in TU Berlin in 1987, and an Associate Researcher in Berkeley in 1989. He was a Guest Professor with the University of Hannover, Hannover, Germany, from 1992 to 1994, and a Guest Researcher with ETHZ in 2000. He is currently a Professor with Fudan University, Shanghai, China. He has authored books *Computer Architecture and RISC Design* (Fudan Press, 2005) and *Analog Integrated Circuit Analysis and Design* (Science Press, 2009). He has authored more than 300 technical papers in analog, mixed-signal, RF integrated circuits, and system-on-chip.

Dr. Hong is currently an Editor for *Journal of Research and Advance of Solid-State Electronics*, the Program Chair of IEEE ASICON in 2005 and 2010, and the ISSCC-TPC Member from 2016 to 2019.